Supporting Information

Revealing the defect-dominated oxygen evolution activity of hematene

Bishnupad Mohanty,[1] Yidan Wei,[3] Mahdi Ghorbani-Asl,[3*] Arkady V. Krasheninnikov,[3,4*] Parasmani Rajput,[5] Bikash Kumar Jena[1,2*]

[1]CSIR-Institute of Minerals and Materials Technology, Bhubaneswar-751013, India.

[2]Academy of Scientific & Innovative Research (AcSIR), Ghaziabad- 201002, India.

[3]Helmholtz-Zentrum Dresden-Rossendorf, Institute of Ion Beam Physics and Materials Research, 01328 Dresden, Germany

[4] Department of Applied Physics, Aalto University School of Science, PO Box 11100, 00076 Aalto, Finland

[5]Atomic & Molecular Physics Division, Bhabha Atomic Research Centre, Trombay, Mumbai-400085, India

*email: bikash@immt.res.in, a.krasheninnikov@hzdr.de, mahdi.ghorbani@hzdr.de

Contents

Experimental Section

Synthesis of hematene (Hm). 30 mg of the pristine hematite (Ht) powder was dispersed in 150 ml of DMF and sonicated in a bath sonicator for 60 h. The solution was centrifuged at lower rpm to remove the bulk particles from the solution. The supernatant having the ultrathin Hm sheets was further centrifuged at a higher rpm of 12000 to settle down it. The sample was separated and dried for further use.

Synthesis of oxygen vacancy hematene (Ov-Hm). The $NaBH_4$ reduction method has been used to create the vacancy of oxygen on as-synthesized Hm.[1,2] 10 mg of the as-synthesized Hm was dispersed in 10 ml of deionized water and sonicated for 45 min. Then, 0.38 g of $NaBH_4$ was added into it, and the stirring was continued for different time 0.5, 1, 1.5, and 2 hours. After that, the solution was centrifuged with water and ethanol at 12000 rpm to collect the samples. The sample was dried in a vacuum oven and kept in a desiccator for prior use.

Synthesis of IrO_2/C. The IrO_2/C colloidal was prepared by using a previously reported process.[3] In detail, 100 mg of potassium hexachloroirridate (K_2IrCl_6) was added to a 50 ml aqueous solution of 0.00063 M sodium hydrogen citrate sesquihydrate. The pH of the solutions was repeatedly adjusted to 7.5 after heating at 95 °C by adding 0.25 M NaOH solutions and the process was repeated until the pH value had stabilized to 7.5. After that 0.184 g of carbon, nanopowder was added to the solutions and ultrasonication for one hour for proper dispersions. After that, the solution was further heated at 95 °C for 2 hours by passing O_2 gas. The sample was dried at 70 °C in a vacuum pump for 12 hours. To remove the organic contaminant, the dried sample was heated at 300 °C for 30 minutes.

Analytical tools. The HRTEM images were taken by using, TITAN G 60-300 transmission electron microscope operating at 300 kV. The phase of the nanostructures was explored by an X'pert PRO (Pan Analytica) X-ray diffraction (XRD) unit using Ni filtered Cu Ka (l ¼ 1.54 °A) radiation, By using Renishaw in Via Raman microscope with a laser wavelength of 514 nm all the Raman analysis was carried out. The elemental composition and oxidations state of the materials was analyzed by X-ray photoelectron spectroscopy (Thermo Fisher Scientific ESCALAB Xi+) with Al-Kα (1486.6eV) as the X-ray source for excitation. All the electrochemical measurements were carried out using CHI-760D electrochemical work station and Bio-Logic instrument (VSP-300). Fe K-edge X-ray absorption near-edge spectroscopy (XANES) and X-ray Absorption Fine Structure (XAFS) were done at in transmission mode the BL-9 of Indus-2 synchrotron source at the RRCAT (Raja Ramanna Centre for Advanced

Technology) Indore, India. This beam line operates in the energy range of 4-25 keV and offers a typical resolution ($\Delta E/E$) of 10^{-4} at 10 keV photon energy. The beam line optics mainly consist of a Rh/Pt coated collimating meridional cylindrical mirror and a Si (111) double crystal monochromator (DCM). For horizontal beam focus, the second crystal was designed as a sagittal cylindrical crystal and another Rh/Pt coated bendable post mirror used for vertical focus. The 300 mm long 3 ionization chambers are used for data collection at the experimental hutch. The DCM energy was calibrated using standard Fe foil at 7112 eV.

XANES and EXAFS analysis. For the analysis of the EXAFS data, the energy-dependent absorption coefficient $\mu(E)$ has been converted to the energy-dependent absorption function $\chi(E)$ and then to the wavenumber dependent absorption coefficient $\chi(k)$. Finally, k^2 weighted $\chi(k)$ spectra were Fourier transformed in R space to generate the $\chi(R)$ versus R spectra in terms of the real distance from the center of the absorbing atoms. The analysis of the EXAFS data have been carried out following the standard procedures[4,5] using the IFEFFIT software package, which includes Fourier transform (FT) to derive the $\chi(R)$ versus R plots from the absorption spectra using ATHENA software, generation of the theoretical EXAFS spectra starting from an assumed crystallographic structure using ARTEMIS software[3] and finally fitting of $\chi(R)$ versus R experimental data with the theoretical ones using the FEFF 6.0 code[4]. By fitting EXAFS data, we minimize R_{factor} in the above process which can be defined by the below formula

$$R_{factor} = \sum \frac{[\mathrm{Im}(\chi_{dat}(r_i) - \chi_{th}(r_i)]^2 + [\mathrm{Re}(\chi_{dat}(r_i) - \chi_{th}(r_i)]^2}{[\mathrm{Im}(\chi_{dat}(r_i)]^2 + [\mathrm{Re}(\chi_{dat}(r_i)]^2} \qquad (1)$$

where, χ_{dat} and χ_{th} represent to the experimental and theoretical $\chi(R)$ values respectively and Im and Re refer to the imaginary and real parts of the respective quantities.

Electrochemical measurements. The electrochemical measurements were carried by using the electrochemical work station in a two-compartment three-electrode electrochemical cell. A platinum wire as the counter, Ag/AgCl as reference electrode and as-synthesized material modified glassy carbon electrodes (GCE, geometric surface area: ~0.071 cm^2) was used working electrode. Prior to the measurement, the GCE was mirror polished with a slurry of alumina powder on a polishing pad, washed with deionized water followed by bath sonication and dried in a vacuum desiccator. A catalyst suspension was prepared by taking 1 mg of

material, 5 µl Nafion (5%) and 95 µl ethanol and sonicate for 30 min. Then, 5 µl of catalyst suspension was drop casted on the GCE electrode and dried in a vacuum desiccator. All the LSV-polarization data were recorded at a scan rate of 5 mV s^{-1}. Initial 30 cycles of cyclic voltammetry scans were used to activate the catalysts. The potentials of all the catalysts converted to the reversible hydrogen electrode (RHE) scale by calibrating the Ag/AgCl reference electrode in H_2-saturated 1 M KOH solution. The reference electrode Ag/AgCl was calibrated by using Pt as the working electrode, Ag/AgCl as reference electrode and Pt wire as counter electrodes. Before the measurement, the Pt electrode are pre-treated with 0.5M H_2SO_4. To corrected the potentials of Ag/AgCl electrode, LSV has been taken at a scan rate of 1 mV/s and the potential at which the current crosses the zero line is taken as the correction factor. As it can be seen in Figure S7, the current crosses the zero line at a potential of -1.035 V. So, the correction factor for the Ag/AgCl reference electrode is 1.035 V.

So, the equation in RHE scale is represented as;

$$E_{RHE} = E_{Ag/AgCl} + 1.035V \quad (2)$$

The charge transfer efficiency of the electrocatalyst is studied by electrochemical impedance spectroscopy (EIS) at an overpotential of 1.53 V by applying the frequency range of 10000 Hz to 1 Hz. All the LSV curves presented here were iR compensated and the potentials denoted as E−iR, where "i" is the current and "R" is the uncompensated ohmic electrolyte resistance determined from the Nyquist impedance measurements. The correction was carried out to get the intrinsic electrocatalytic activity of the electrode by eliminating the negative influence of the electrolyte and catalyst resistance on electrochemical behaviour. Further, the Tafel plots were obtained from the polarization curves and the slope are calculated by linear fitting by using the equation,

$$\eta = a + b \log j \quad (3)$$

Here η, a, b and j were denoted as the overpotential, Tafel constant, the Tafel slope, and the current density. For OER, the overpotential (η) of the catalysts was calculated by using the following equation.

$$\eta = E \text{ (vs. RHE)} - 1.23V \quad (4)$$

The durability of the sample was verified by modifying the sample ink on the well-polished GC plate using the chronopotentiometry and cyclic voltammetry technique.

Electrical double layered capacitance measurement. By using nonaqueous aprotic electrolyte (KPF_6–CH_3CN) the electrochemical accessible surface area (ECSA) of all the electrocatalysts was derived from the double-layered capacitance (C_{dl}) values on the basis of cyclic voltammetry.[6,7] The catalyst was modified on the glassy carbon electrode (GCE). The cyclic voltammograms were recorded in a non-Faradic region (0 to 0.1 V vs. Ag/AgCl) at various scan rates of 10, 20, 40, 60, 80, 100 mV/s. The current is directly proportional to the scan rates per the following equation 4.

$$i = \nu C_{dl} \quad (5)$$

Here, the C_{dl} was derived from the average value of linear fitted slope obtained from the plot of both the anodic and cathodic current at 0.05 V against the scan rates. Then, the electrochemical surface area (ECSA) has been calculated as per the following equation 5.

$$ECSA = C_{dl}/ Cs \quad (6)$$

The Cs is the specific capacitance and the value of Cs is 0.04 mF cm^{-2}. By simply dividing the geometrical surface area (0.071 cm^2) of the working electrode the R_f value can be calculated.

Mass activity. The mass activity (A g^{-1}) of all the catalysts are derived at η = 300 mV by using the equations

$$\text{Mass activity} = j/m \quad (7)$$

Where j is the current density ($mAcm_{geo}^{-2}$) and m is catalyst loading (0.7 $mgcm_{geo}^{-2}$)

Turnover frequency (TOF). The turnover frequency (TOF) was estimated by the equation:

$$TOF = j \times M /4 \times F \times m \quad (8)$$

where j is the current density, F is Faraday constant (96485 C mol^{-1}), M is the molar mass, m is the loading mass, and 4 is the needed electron number for one molecule of O_2.

Rotating ring disk electrode (RRDE) voltammetry. RRDE experiments were carried out using a VSP-300 multi-channel potentiostat (Biologic Inc), a rotator, GC Disk-Pt Ring of Pine instruments USA. The disk electrode was scanned at a rate of 10 mV s^{-1} and the ring electrode potential was set to 1.48 V versus RHE. The hydrogen peroxide yield (H_2O_2 %), the electron transfer number (n) and Faradic efficiency (FE) were determined by the following equations:[8,9]

$$H_2O_2(\%) = 100\frac{2 \times \frac{I_r}{N}}{I_d + \frac{I_r}{N}} \quad (9)$$

$$n = 4 \times \frac{I_d}{I_d + \frac{I_r}{N}} \quad (10)$$

$$FE = \frac{I_r}{N \times I_d} \quad (11)$$

where I_d represents the disk current, I_r is the ring current and N = ~ 0.2 stands for the current collection efficiency of the Pt ring.

Mott-Schottky (M-S) analysis. The M-S plots are derived from electrochemical impedance measurements. we conducted capacitance measurements at 10 kHz frequency. M-S analysis was carried out to estimate the donor density (Nd), flat band potentials (V_{fb}), Debye radius (L_D) of all the catalysts. The Nd, $V_{fb,}$ and L_D have estimated form Mott-Schottky plots by using the equation. [10,11]

$$\frac{1}{C^2} = \frac{2}{eA^2 N_d \epsilon \epsilon_0} \left(V - V_{fb} - \frac{KT}{e}\right) \quad (12)$$

$$N_d = \frac{2}{e\epsilon\epsilon_0} \left[\frac{dE}{d\left(\frac{1}{C^2}\right)}\right] \quad (13)$$

$$L_D = \sqrt{\left(\frac{\epsilon\epsilon_0 KT}{2e^2 N_d}\right)} \quad (14)$$

where C and A represent the interfacial capacitance and area, respectively, V is the applied voltage, k is the Boltzmann's constant, T is the absolute temperature, e_0 is the electron charge (1.602×10^{-19} C), ϵ is the dielectric constant of α-Fe_2O_3 (80), ϵ_0 is the permittivity of vacuum (8.854×10^{-12} Fm^{-1}). The flat band potential can be measured by extrapolation of the linear fitted curve to the X-axis at a point $1/C^2 = 0$.

Computational details. The density functional theory calculations have been performed based on generalized gradient approximation (GGA) with Perdew-Burke- Ernzerhof (PBE) for exchange-correlation function as implemented in VASP code[12–15]. We performed DFT+U calculations for high electronic correlation effects that regular DFT exchange-correlation (XC) functional approximations fail to represent. An effective U value of 4 eV that was found for Fe atoms by comparing the band gap values of Fe_2O_3 bulk with the experimental one. All other atoms were not given explicit orbital corrections, that is, U = 0. Projected augmented plane

wave (PAW) potentials were used to represent the frozen core electrons and nuclei of each atom: [Ar]$3d^6$ $4s^2$ shells in Fe atoms, [He] shells in O atoms. A plane-wave basis set with an energy cutoff of 550 eV is used. The Brillouin zone of the supercells was sampled using 8 × 8 × 1 k-points for optimization according to the scheme proposed by Monkhorst and Pack[16]. A geometry relaxation was performed up to a tolerance of 0.01 eV/Å for atomic forces. Bulk Fe_2O_3 was calculated with a hexagonal 30-atom unit cell with long-range antiferromagnetic ordering. We have used 2×2 supercells to simulate slab models of the (001) and (104) facets, as shown in Figure S6-S10. A vacuum layer of around 20 Å was inserted in the direction perpendicular to the surfaces to diminish the spurious inter-layer interaction.

Surface energy:

The surface energy (γ) of exfoliated hematite facets from its bulk counterparts is calculated according to the following formula:[17]

$$r_{\mu_O} = \frac{1}{2A}\left[\left(\frac{3}{2}N_{Fe} - N_O\right)\mu_O + \left(E(N_O, N_{Fe}) - \frac{1}{2}N_{Fe}\mu_{Fe_2O_3}\right)\right] \quad (15)$$

where A represents the surface area and $E(N_O, N_{Fe})$ is the total energy of the symmetric surface model. N_{Fe} and N_O are the number of Fe and O atoms in the surface model, μ_O and $\mu_{Fe_2O_3}$ stand for the corresponding chemical potential of oxygen and bulk Ht, respectively. The factor of 2 accounts for two identical surfaces.

Vacancy formation energy:

The formation energy of oxygen vacancy is calculated as

$$E_f = E_{defect} - E_{perfect} + \mu_O \quad (16)$$

where E_{defect} is the total energy of a relaxed supercell containing vacancies, $E_{perfect}$ is the total energy of the perfect host crystal and μ_O is the chemical potential of oxygen (gas).

Free energy profile for OER:

In the alkaline medium, the OER can proceed via the following steps:[18]

I: $* + OH^- \longrightarrow A - OH + e^-$

II: $* - OH + OH^- \longrightarrow * - O + e^- + H_2O$

III: $* - O + OH^- \longrightarrow * - OOH + e^-$

IV: $* - OOH + OH^- \longrightarrow * - O_2 + e^- + H_2O$

V: $* - O_2 \longrightarrow * + O_2$ (Gas form)

The overpotential of OER is defined as:

$$\eta^{OER} = \frac{Max\,[\Delta G_I, \Delta G_{II}, \Delta G_{III}, \Delta G_{IV}, \Delta G_V]}{e} \quad (17)$$

where ΔG_i represents the variations of the free energy at the i*th* reaction step. Gibbs free energy change (ΔG) of each reaction step is evaluated based on computational hydrogen (CHE) electrode model.[13]

$$\Delta G = \Delta E + \Delta E_{ZPE} - T\Delta S + \Delta G_{Uext} + \Delta G_{pH} \quad (18)$$

where ΔE is the reaction energy directly computed from the DFT calculations. The energies of O and OH species have been taken from the experimental value of the OER reaction in alkaline medium.[13] The zero-point energy corrections (ΔE_{ZPE}) and the entropy changes (TΔS) are obtained from vibrational frequency calculations and standard tables for gas-phase molecules. $\Delta G_{Uext} = -neU$ represents the effect of the external potential for the electrochemical step, where *n* is the number of transferred electrons and *U* is the electrode potential relative to the standard hydrogen electrode. ΔG_{pH} stands for the free energy change of H^+ at $pH \neq 0$.[13]

Atomic force microscopy (AFM) Analysis

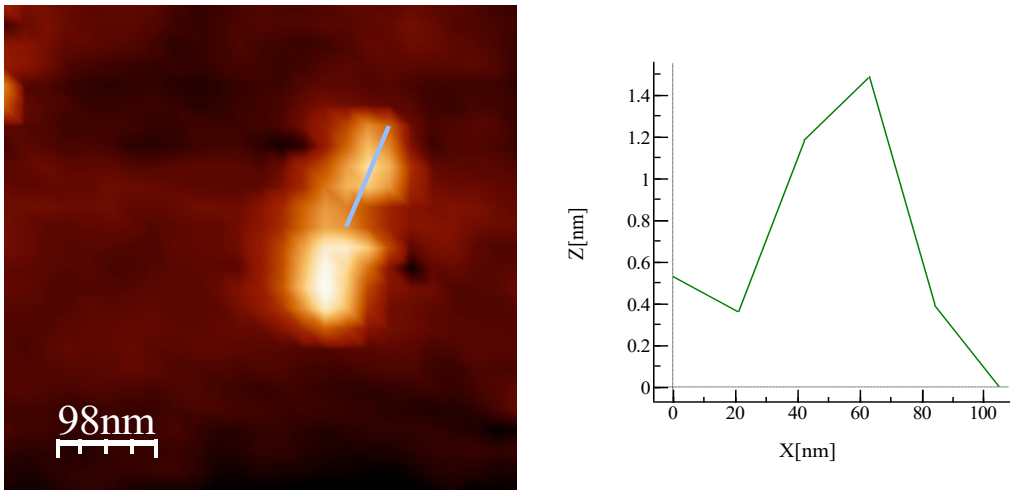

Figure S1. (a) Atomic force microscopy (AFM) image of as synthesised Hm, (b) corresponding height profile.

X-ray Diffraction Analysis:

The XRD pattern of Ht and Hm are shown in figure S1. All the diffraction peak of Hm is perfectly matched with Ht (JCPDS card 33-664, a = 5.035Å and c =13.74 Å). No additional peaks are formed that indicate the absence of impurities like β-FeOOH, Fe_3O_4, and γ-Fe_2O_3. In comparison to Ht, the diffraction peaks of Hm are upshifted and broadened. This is maybe due to the increase in strain or increase in lattice defect in the Hm.[19]

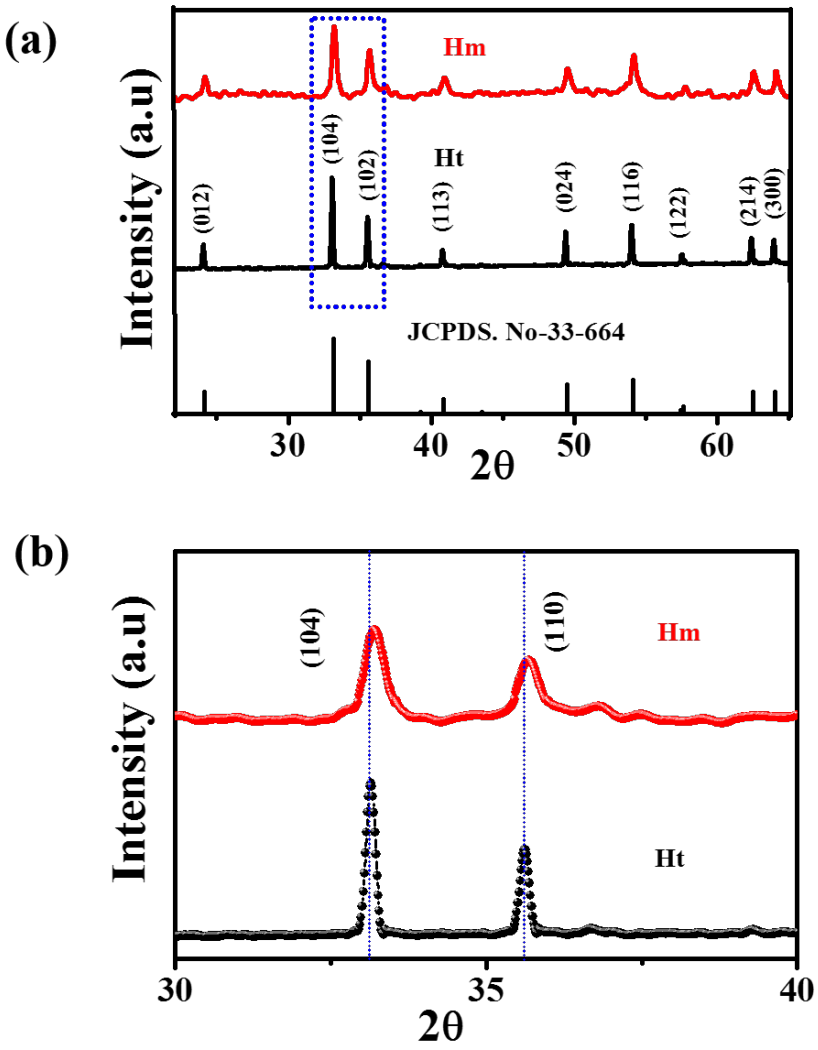

Figure S2. (a) XRD pattern of Ht and Hm. (b) Enlarge spectra of (104) and (110) plane.

Raman Analysis:

The overlap Raman spectra of Ht and Hm are shown in Figure S2. In the case of Ht, the Raman spectrum in the wavenumber range of 200–1800 cm^{-1} is dominated by six dominated peaks are located at 222.9, 290.6, 405.5, 494, 605.9 and 1302 cm^{-1}. The peaks at 222.9, 494 cm^{-1} correspond to the A_g, the bands at 290.6, 405.5, 605.9 cm^{-1} are assigned to E_g modes of vibrations[20]. The peak at around 1302 cm^{-1} is attributed to two-magnon scattering, which arises from the antiparallel close spin site interaction of two-magnons.[21] All the results are a good agreement with previous reports.[22] Similarly, in the case of Hm, along with all the peak of Ht an additional peak is located around 655 cm^{-1} and this is a forbidden vibrational mode in the Raman spectra and assigned to Eu. This type of mode originates from disorder within the crystal lattice. The change in intensity ratio and shift in vibrational modes are also observed in Hm.

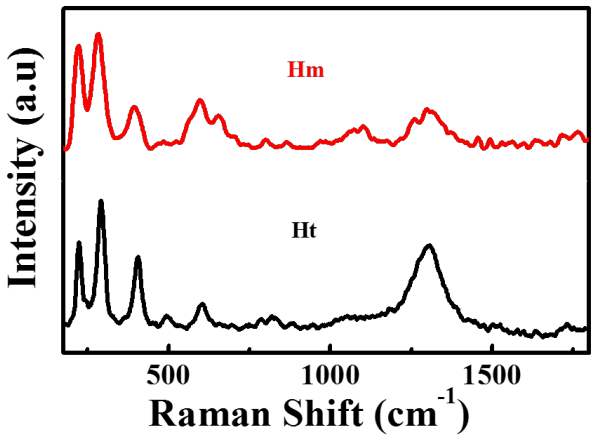

Figure S3. Raman spectrum of Ht and Hm.

X-ray photoelectron spectroscopy (XPS) Analysis:

For elemental analysis, X-ray photoelectron spectroscopy (XPS) characterization is carried out. Figure S3a is the overlap full XPS spectrum of Ht and Hm. Both the spectrum showing the absence of other metal impurities i.e. Ht is consisting of elements Fe and O. Figure S3b showing the Fe 2p XPS spectra of both Ht and Hm. In Ht two peaks at around 710.3 and 724.1 eV are observed in the Fe 2p region, which can be assigned to Fe $2p_{3/2}$ and Fe $2p_{1/2}$, respectively and two peaks are separated by 13.8 eV. In comparison to Fe $2p_{1/2}$ peak, Fe $2p_{3/2}$ peak is narrower and stronger also the area under the curve is also higher. This is due to spin-orbit coupling.[23] The satellite peak for Fe $2p_{3/2}$ is located at 718.9 eV, which is located 8 eV higher than Fe $2p_{3/2}$ peak. This satellite suggests that in Ht Fe is in Fe^{+3} state. The satellite for Fe $2p_{1/2}$ is located at 732.8 eV. In the case of Hm, both Fe $2p_{3/2}$ and Fe $2p_{1/2}$ are shifted towards higher binding energy and two peaks are separated by 13.7 eV. Two satellite peaks are located at 719.6 and 733.8 eV. This confirms that the oxidation state of Fe in Hm is not changed. In O 1s XPS spectra of both Ht and Hm two peaks are observed. The peak centered at 529.5 eV correspond to the lattice oxygen and the peak cantered at 531.5 eV correspond to the defect's oxygen in the metal's oxides. In Hm, the peak cantered at 531.5 eV have a higher intensity that suggests that Hm have more defect's oxygen or increased in concentrations of undercoordinated surface oxygen atoms and this may be due to ultrathin 2D morphology.[24] This increased in concentration of undercoordinated surface oxygen atoms are responsible for enhancing the electrocatalytic OER activity. [25]

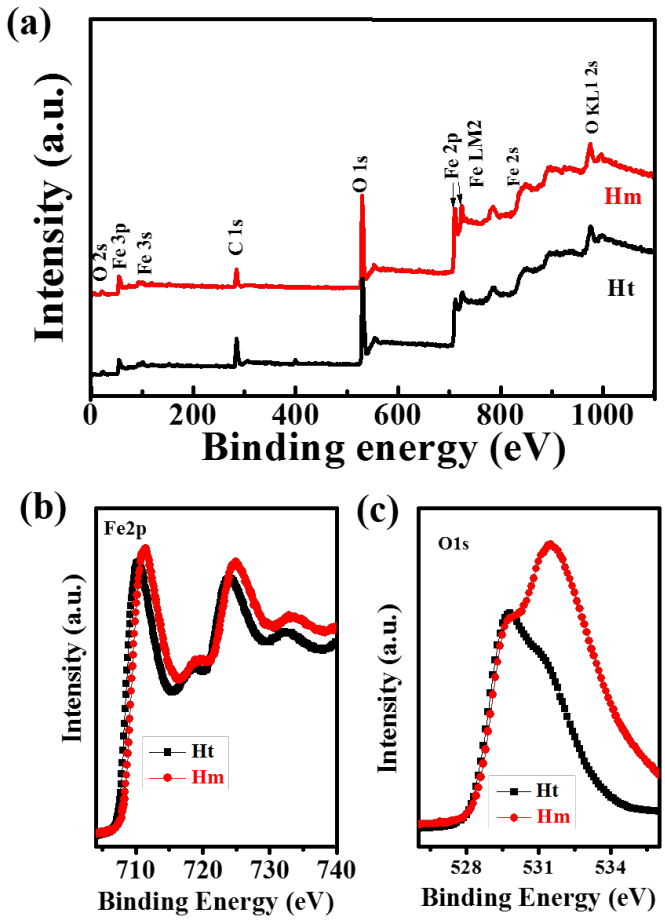

Figure S4. (a) Full XPS spectra of Ht and Hm (b) Fe 2p XPS spectra of Ht and Hm (c) O 1s XPS spectra of Ht and Hm.

Raman Analysis after oxygen vacancy:

Raman analysis is also carried out after creating oxygen vacancies. Figure S4 is the overlapping Raman spectrum of before and after vacancies, i.e. Hm and Ov-Hm. All the Raman spectrum of Ov-Hm is well-indexed with Hm and shifted towards lower wavenumber.[26]

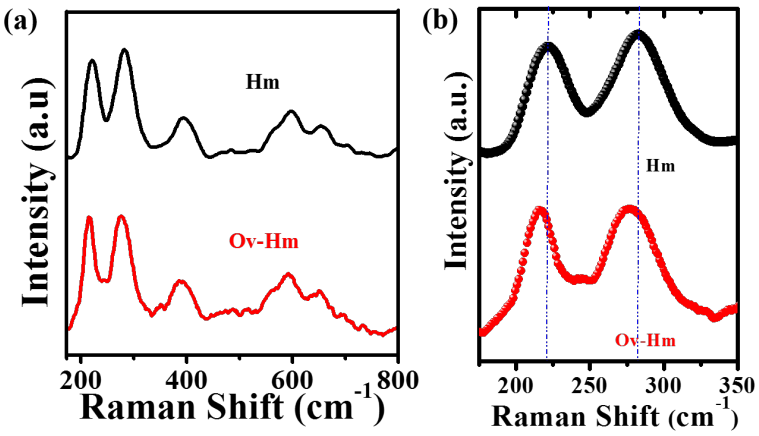

Figure S5. (a) Raman Data of Hm and Ov-Hm, (b) Zoom Raman Data of Hm and Ov-Hm

Mott−Schottky plot

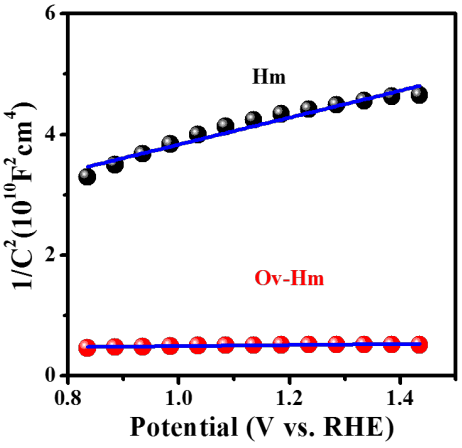

Figure S6. (a) Mott−Schottky plots of Hm and Ov-Hm samples obtained at each potential with 10 kHz frequency in the dark in a 1 M KOH electrolyte.

XAFS fitting data

Table S1. Structural parameters derived from fitting of XAFS data of all samples: Bond distance (R) and Debye-Waller Factor (σ^2). The numbers in parentheses indicate the uncertainty in the last digit.

Sample Name	$CN_{Fe\text{-}O1}$	$R_{Fe\text{-}O1}$ (Å)	$\sigma^2_{Fe\text{-}O1}$ (Å^2)	$CN_{Fe\text{-}O2}$	$R_{Fe\text{-}O2}$ (Å)	$\sigma^2_{Fe\text{-}O2}$ (Å^2)	$CN_{Fe\text{-}Fe}$	$R_{Fe\text{-}Fe}$ (Å)	$\sigma^2_{Fe\text{-}Fe}$ (Å^2)
Ht	3	1.941 (3)	0.0030 (3)	3	2.114 (4)	0.0035 (3)	4	2.931 (3)	0.0063 (4)
Hm	3.2 (2)	1.950 (4)	0.0045 (4)	3.1 (2)	2.122 (3)	0.0047 (4)	3.2 (3)	2.947 (3)	0.0067 (5)
Ov-Hm	2.5 (2)	1.955 (4)	0.0061 (3)	2.0 (2)	2.121 (4)	0.0079 (4)	3.6 (3)	2.942 (4)	0.0075 (5)

Calibration of Reference Ag/AgCl Electrode

The potentials of all the catalysts converted to the reversible hydrogen electrode (RHE) were scaled by calibrating the Ag/AgCl reference electrode in H_2-saturated 1 M KOH solution. The reference electrode Ag/AgCl was calibrated by using Pt as the working electrode, Ag/AgCl as reference electrode and Pt wire as counter electrodes. Before the measurement, the Pt electrode was pre-treated with 0.5M H_2SO_4. To correct the potentials of Ag/AgCl electrode, LSV has been recorded at a scan rate of 1 mV/s and the potential at which the current crosses the zero line is taken as the correction factor. As evident from Figure S19, the current crosses the zero line at a potential of -1.035 V. So, the correction factor for the Ag/AgCl reference electrode is 1.035 V.

So, it is represented as;

$$E_{RHE} = E_{Ag/AgCl} + 1.035V$$

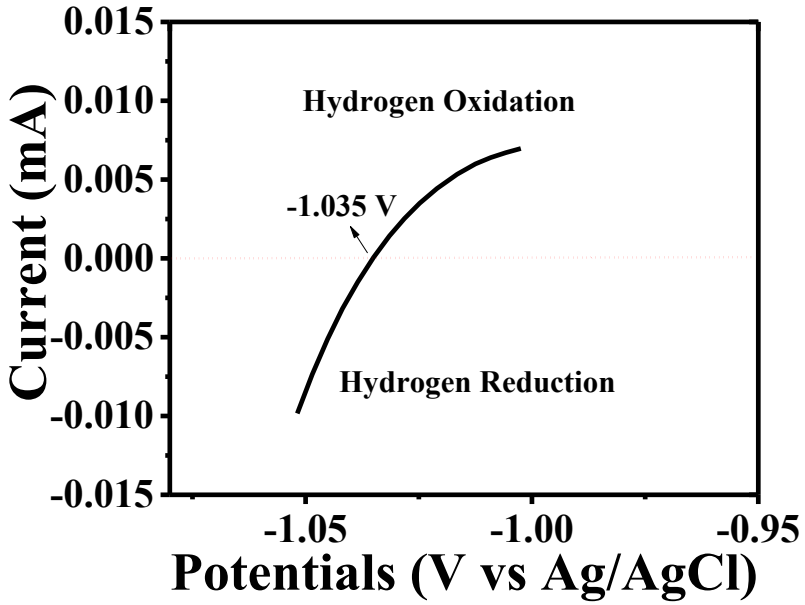

Figure S7. LSV showing the calibration of the Ag/AgCl reference electrode in 1 M KOH solution.

iR-corrected LSV data

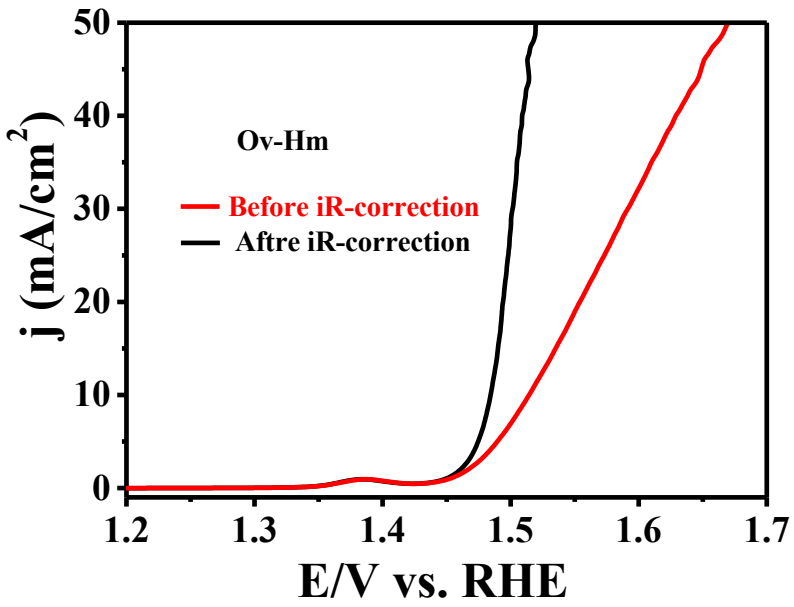

Figure S8. LSV of Ov-Hm before and after iR- correction.

OER Analysis at Different Reduction Time:

The electrocatalytic performance of Ov-Hm exhibits dependency on the reduction time. For tuning and optimizing the OER activity, Hm is reduced for different time (0.5h, 1 h, 1.5h, 2h). The LSV of Hm with different reductions times is shown in figure S6a. As shown, the one-hour reduced sample is named as Ov-Hm and possesses much higher OER activity with lower overpotentials. Interestingly, Ov-Hm shows the largest negative shift with an onset overpotential 210 mV. Similarly, Ov-Hm-0.5h, Ov-Hm-1.5h and Ov-Hm-2h exhibiting the onset overpotential of 230, 225, 240 mV respectively. The overpotentials (η) that needed to achieve the current density of 10 mA/cm^2 are 269, 250, 263, and 271 mV for the electrocatalysts prepared using 0.5, 1, 1.5, and 2-hour treatment respectively. figure S7c exhibit the corresponding Tafel slope of the catalysts. Ov-Hm-0.5h, Ov-Hm-1.5h and Ov-Hm-2h exhibiting the Tafel slope of 42, 38, and 47 mV/dec respectively.

X-ray diffraction analysis was also carried out to check the phase transition in Hm after 1h and 2h reductions and presented in figure S6c. The XRD pattern shows that after 1h reduction there are no phase transitions i.e. all the XRD plane of 1h reduced Hm is well-indexed with Hm. This clarifies that the enhancement in OER activity is not due to phase transitions but due to the oxygen vacancies.

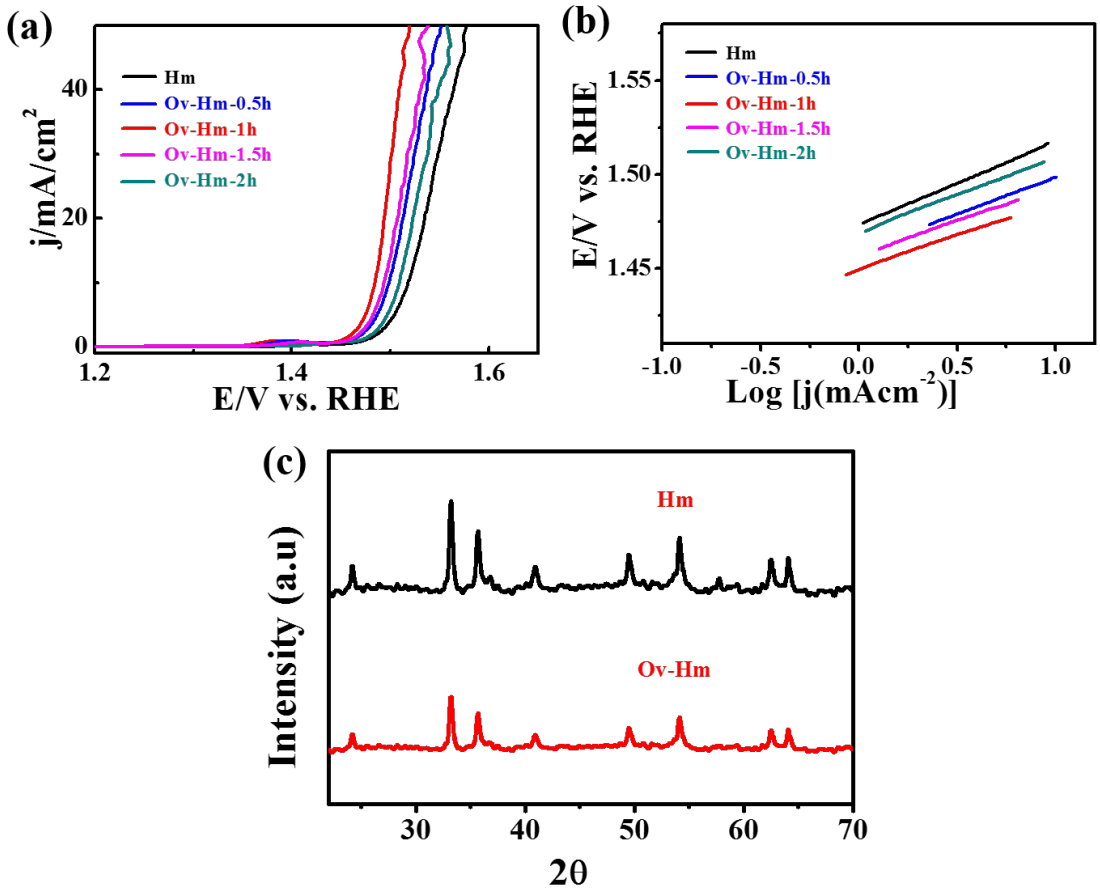

Figure S9. (a) LSV curve of Hm with different reductions time. (b) Corresponding Tafel slope. (c) XRD data of before and after reductions.

2.5 Cyclic voltammetry response of redox of Fe (II)/Fe (III) pair.

In the OER polarization curve, a small oxidation peak was observed for Ov-Hm at a potential of ≈1.38 V that may be assigned to the Fe (II)/Fe (III) oxidation and exhibit much earlier compared to Hm (≈1.42 V). The cyclic voltammetry (CV) has been carried out to understand the significance of the observed peak (Figure S7). In the cyclic voltammetry (CV) redox peak was observed in both Hm, Ov-Hm. In Ov-Hm the Fe (II)/ Fe (III) redox pair at 1.38 V (anodic) and 1.28 V vs. RHE is formed. Similarly, Hm Fe (II)/ Fe (III) redox pair 1.42 V (anodic) and 1.31 V (cathodic) vs. RHE is formed. In Ov-Hm the redox peak is shifted catholically with a higher area than Hm. This suggested the faster ion transfer in the Ov-Hm surface.[27]

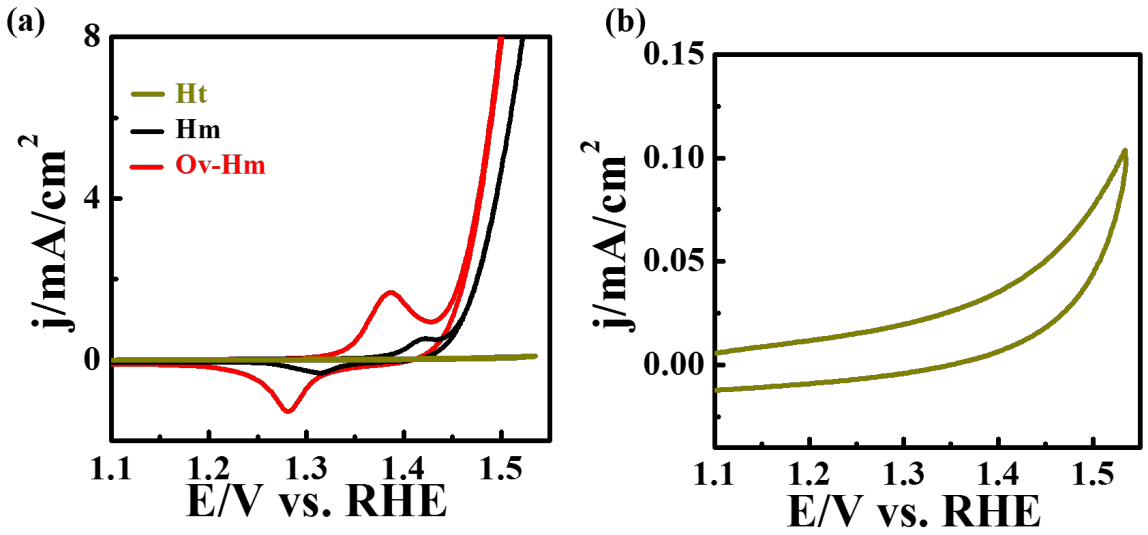

Figure S10. (a) Cyclic voltammetry response of Ov-Hm, Hm and Ht. The peak at ~1.4 V (vs. RHE) corresponds to the redox of Fe (II)/Fe (III) pair. (b) Cyclic voltammetry response of Ht (enlarged).

Performance comparison with previous literatures

Table S2: Performance comparison of Ov-Hm with other reported materials in previous literature towards OER application.

No.	Sample	η @10 mA cm^{-2} mV	Tafel slope mV/dec	Electrolyte	Reference
1	Pure α-FeOOH	580	77	1MKOH	ACS Omega 2018, 3, 7840−7845
2	δ-FeOOH NSs/NF	265	36	1MKOH	Adv. Mater. 2018, 1803144
3	Fe/Fe_3C–F@CNT	286	49	1MKOH	J. Mater. Chem. A, 2018, 6, 21577–21584
4	CP@FeP	350	64	1MKOH	Chem. Comm. 2016, 52, 8711-8714
5	Fe/Fe_2O_3@Fe-N-C	540	77.5	0.1MKOH	Nano Res. 2016, 9, 2123-2137.
6	α-Fe_2O_3 NA/CC	420	52	0.1MKOH	Electrochem. Commun. 2014, 49, 21-24
7	$Co_{0.20}Fe_{0.80}OOH$	380	40	1MKOH	ACS Omega 2018, 3, 7840−7845
8	$Co_xFe_{3-x}O_4$ film	420	53	1 MNaOH	ectrochim. Acta 2016, 210, 942–949.
9	$Co_{0.5}4Fe_{0.46}OOH$	390	47	0.1MKOH	Sci. Rep. 2017, 7, 43590
10	Fe_3O_4 NPs	-	295	0.1MKOH	Applied Nanoscience (2018) 8:1427–1435
11	Fe_3O_4@ NiSx/rGO-0.04	330	35.5	1M KOH	https://doi.org/10.1016/j.apsusc.2018.02.097
12	Fe_2O_3/CNT	410	62	1M KOH	http://dx.doi.org/doi:10.1016/j.electacta.2016.11.107
13	α-Fe_2O_3 (012) facet nanocrystals	317	58.5	1M KOH	Adv. Mater. 2018, 1804341
14	$CoFe_2O_4$	490	54.2	1M KOH	Electrochemistry Communications 87 (2018) 1–4

15	c-Fe_2O_3	650	56	1M KOH	Journal of Catalysis 365 (2018) 29–35
16	$Fe_1Co_1O_x$	250	36	1M KOH	Nano Research 2018, 11(6): 3509–3518
17	Amorphous $Fe_{0.5}Co_{0.5}Ox$	257	30.1	1M KOH	Adv. Mater. 2017, 1701410.
18	Fe_2O_3/P–S-GC	-	55	1M KOH	RSC Adv., 2016, 6, 64258–64265
19	$Ni_{0.71}Fe_{0.29}$ (OH)x/ graphite	296	58	1M KOH	Nanoscale, 2016,8, 5015-5023
20	S-$NiFe_2O_4$/NF	267	36.7	1M KOH	Nano Energy 2017, 40, 264.
21	FeOOH	500	-	0.5 M borate buffer	J. Mater. Chem. A 2016, 4, 3655
22	FeOOH	470		1.0 M NaOH	J. Mater. Chem. A 2016, 4, 3655
23	Amorphous Fe_2O_3	>400	40	0.1 M KOH	Science 2013, 340, 60
24	α-Fe_2O_3	>470	40	0.1 M KOH	Science 2013, 340, 60
25	Amorphous FeOx	410	40	0.1 M KOH	J. Am. Chem. Soc. 2013, 135, 11580
26	FeSx	390	-	0.1 M KOH	Adv. Energy Mater. 2016, 6, 1502095
27	Spinel Co3O4	300	129	1.0 M KOH	J. Am. Chem. Soc. 2016, 138, 36.
28	MoS_2 QDs	370	39	1.0 M KOH	ACS Catal., 2018, 8 (3), pp 1683–1689
29	N-Co_9S_8/G	409	82.7	1.0 M KOH	Energy Environ. Sci. 2016, 9, 1320–1326
30	CoS_2/N,S-GO	380	75	1.0 M KOH	ACS Catal. 2015, 5, 3625– 3637.
31	Ni_3FeN nanoparticle	280	46	1.0 M KOH	Adv. Energy Mater. 2016, 6, 1502585.
32	$NiCo_2O_4$ nanotubes	290	-	1.0 M KOH	Angew. Chem. Int. Ed. 2016, 55, 6290.

33	Ni-Fe hydroxides /N-graphene	337	45	1.0 M KOH	Adv. Mater. 2015, 27, 4516.
34	S-$NiFe_2O_4$/NF	267	36.7	1.0 M KOH	Nano Energy 2017, 40, 264
35	CoOOH NSs	300	38	1.0 M KOH	Angew. Chem. Int. Ed. 2015, 127, 8846
36	Ni-Fe hydroxides /N-graphene	337	45	1.0 M KOH	Adv. Mater. 2015, 27, 4516
37	Mesoporous CoPi	380	58.7	1.0 M KOH	Small 2016, 12, 1709–1715.
38	α-FeCoOx	300	-	1.0 M KOH	J. Am. Chem. Soc. 2015, 137, 3638
39	NiFe LDH	300		1.0 M KOH	J. Am. Chem. Soc. 2015, 137, 1305
40	Mn3O4/CoSe2 hybrid	450	49	0.1 M KOH	J. Am. Chem.Soc. 2012, 134, 2930
41	Co3O4/NiCo2O4 DSNCs	340	88	1.0 M KOH	J. Am. Chem. Soc. 2015, 137, 5590
42	Ni-Co binary oxides	325	39	1.0 M KOH	J. Am. Chem. Soc. 2014, 136, 7551.
43	Mn_xO_y/NC	450	83	0.1 M KOH	Small 2014, 10, 2251.
44	Co_9S_8@NOSC-900	340	68	1.0 M KOH	Adv. Funct. Mater. 2017, 27, 1606585
45	Hm	280	43	1.0 M KOH	This work
46	Ov-Hm	250	34	1.0 M KOH	This work

LSV polarisations curve at different pH

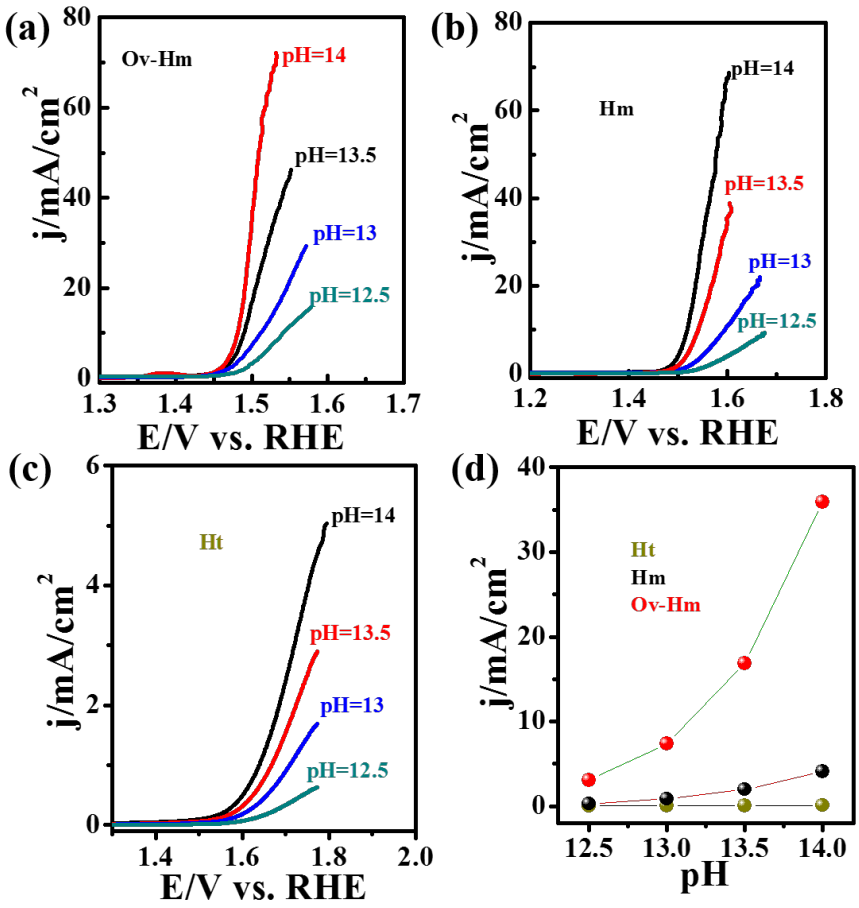

Figure S11: pH dependence of the OER activities (a) Ov-Hm, (b) Hm and (c) Ht (d). Current densities of Ov-Hm, Hm and Ht at 1.5 V versus RHE as a function of the pH value.

Electrochemical Active Surface Areas (ECSA), Turn Over Frequency (TOF), Mass Activity (MA):

The ECSA was estimated from the double-layer capacitances (C_{dl}) (by taking non-aqueous aprotic KPF_6–CH_3CN electrolyte,[6,7] which were derived from the series of scan rate of cyclic voltammetry (CV) at the non-Faradaic potential window and presented in Figure S9. The Cdl value is calculated from the linear plot of current density vs. scan rate by using equation $i = \upsilon C_{dl}$ (Figure S9). The C_{dl} value of Ov-Hm is 0.96 mF, which is higher than that of Hm (0.52 mF) and Ht (0.032 mF). Since ECSA is directly proportional to C_{dl} value and the value of ECSA are calculated from the equation $ECSA = C_{dl}/Cs$, (Where Cs = 0.04 mF). The ECSA of all the catalysts are summarised in Table S2, and it suggests that the Ov-Hm catalyst has a large active surface area. As like ECSA, the roughness factor (R_f) is also an important parameter that represents the catalytic interface texture. R_f is calculated from ECSA by dividing the geometrical surface area. The R_f value of Ov-Hm is 338, which is nearly two times higher than Hm (185) and 30 times higher than Ht (11.26). The higher ECSA and R_f value of Ov-Hm indicate the presence of abundant active sites and favourable reaction kinetics. Further, the intrinsic activities of the above catalysts were estimated from the turnover frequency (TOF) analysis. The TOF value of Ov-Hm is estimated to be 0.033 s^{-1} (at η = 300 mV) which is higher than that of Hm (0.010 s^{-1}) , and Ht is (0.00087 s^{-1}). This higher TOF value of Ov-Hm confirms the abundance of inherent catalytic activity sites. The mass activity of all the catalysts also estimated (η = 300 mV) and compared. All the data are summarised in Table S3, and presented in Figure 4(d). The above observation supports the enhanced activity of Ov-Hm due to its ultrathin 2D nature and rich of active defect sites.

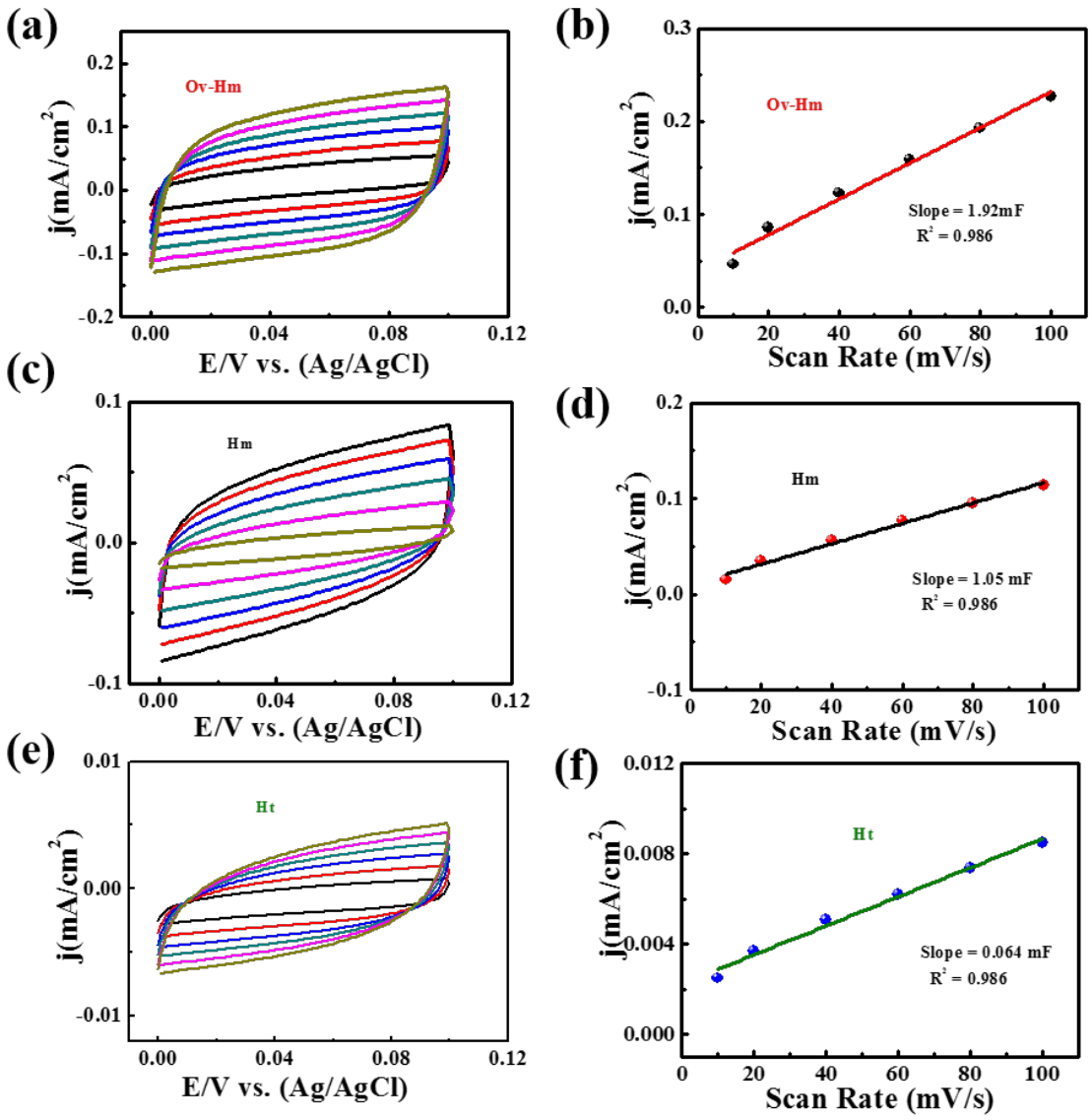

Figure S12. Cyclic voltammograms obtained from the non-Faradic Region of as-synthesized materials at scan rates of 10-100 mV in nonaqueous aprotic KPF_6–CH_3CN electrolyte. The corresponding plot of scan rate vs the anodic current measured at 0.0.05V.

Summarized OER Performance data

Table S3 Summarized OER performance data of as-synthesized materials

Catalysts	Cdl (mF/cm^2)	ECSA	R_f	Mass Activity	TOF (s^{-1}) η=300 mV	R_{ct} (Ω)	Tafel Slope (mV/dec)
Ov-Hm	0.96	24	388	82	0.033	24	34
Hm	0.52	13	183	25	0.010	80	43
Ht	0.032	0.8	11.26	0.27	0.00087	762	114

Impedance Analysis:

Charge transfer between the catalyst and electrolyte was an important indicator to evaluate the catalytic properties, and electrochemical impedance spectroscopy (EIS) is a useful technique to estimate the charge transfer feasibility and reaction of electrode-electrolyte interfaces during the OER process. The electrochemical impedance spectroscopic (EIS) of all the catalysts are recorded at a frequency range of 10^5–10^{-1} Hz at the overpotentials of 300 mV in the potentiostat mode. The corresponding Nyquist plots are presented in Figure S10. By fitting the EIS spectra with a simplified equivalent circuit, the charge transfer resistance (Rct) was obtained from the Nyquist plots and summarized in Table S3. The charge-transfer resistance (R_{ct}) of Hm is ≈ 80 Ω, which is much lower than that of Ht (≈ 762 Ω) suggesting a much faster charge transfer rate and accelerated kinetics for OER. The R_{ct} value of Ov-Hm (≈ 24 Ω) is further decreased and demonstrating much higher electrical conductivity and OER kinetics. Thus, superior OER activity of Ov-Hm is attributed to the high intrinsic electrical conductivity and enhanced OER kinetics.

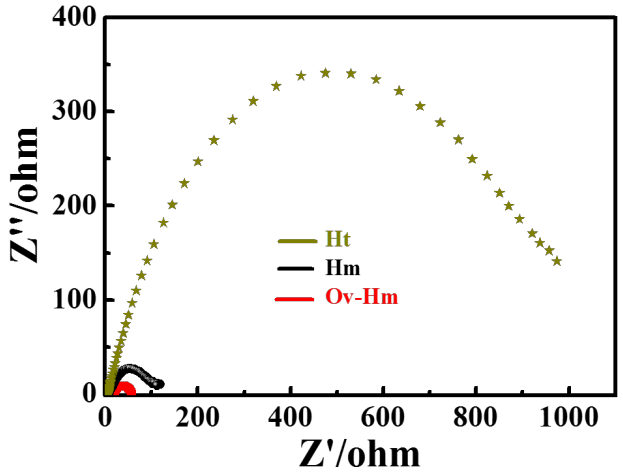

Figure S13. EIS Nyquist plots of Ov-Hm, Hm and Ht.

Mott-Schottky analysis to understand the charge transfer at electrode and electrolyte interface:

To understand the charge-transfer between the electrocatalyst and electrolyte was an important indicator to evaluate the catalytic properties. Electrocatalytic properties of all the catalysts were explored at the interface of electrolyte-electrode in alkaline medium by using Mott-Schottky analysis. When electrode materials are contacted with the electrolyte, at the interface minor potentials difference is created between electrode materials and electrolytes. As a result, the system can reach the equilibrium through the transfer of an electron from higher potential to the lower potentials, i.e. electrode materials to the electrolyte. As a result, equilibrium is maintained at the interface, and the Fermi levels for both phases are comparable.[10] Due to this equilibration, the depletion layer is formed, and it depends on the difference between the Fermi level and the electrolyte. The region where the depletion layer formed is called the space charge region (Figure S11). At the depletion width, the electrode materials have an excess positively charged, which is counterbalanced by the negative charge in the Helmholtz layer of the electrolyte close to the electrode. By applying external bias causes the band bending of electrode, and it depends on the applied voltage. The applied bias having no band bending, i.e. no space charge layer or the potential drops between the surface and the bulk of the electrode to zero; the semiconductor is in flat band potentials. Different electrode materials possess different charge-transfer ability and it depends on the position of valence and conduction band.

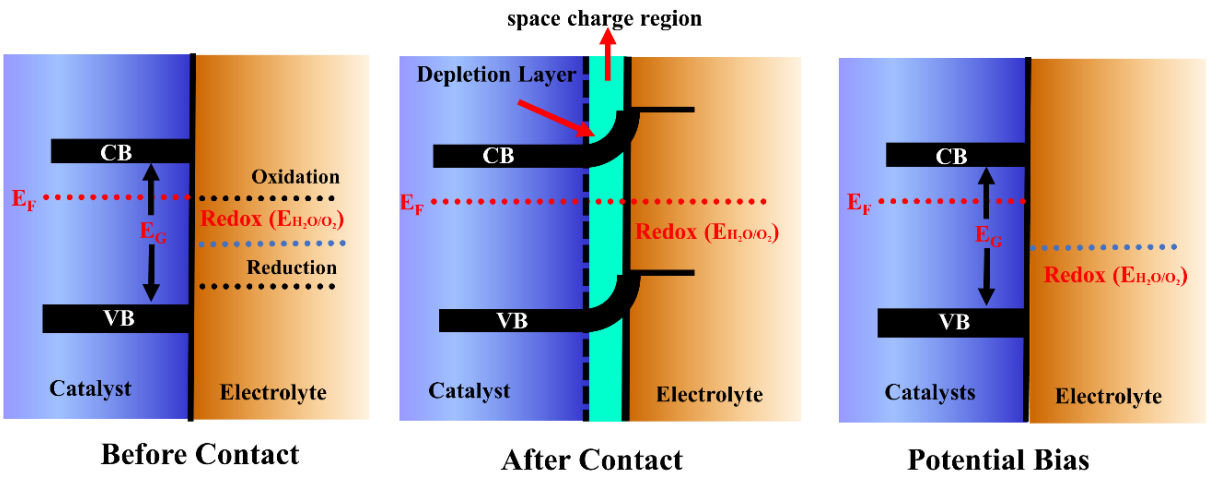

Figure S14. Conduction and Valence band behaviour in electrode and electrolyte interface: a) before contact, b) after contact, c) under potential bias.

The Mott-Schottky plot of all the electrode materials shown in Figure S12. The linear fit of Mott–Schottky plots gives the positive slopes of all the electrode materials, i.e. Ht, Hm, and Ov-Hm which indicates that they are n-type semiconductors with electrons as majority carriers. The flat band potential (V_{fb}), Donor density (N_d) and Debye radius (L_D) are calculated by using the equations S11, S12, S13 and value of all the electrode materials are summarized in the Table S4. Ht exhibiting higher positive V_{fb} value with lower donor density N_d. The higher V_{fb} and poor N_d of Ht make it unsuitable not only for photocatalytic properties but also for electrocatalytic activity. After decreasing the thickness and creating oxygen vacancies in the Ht, Hm and Ov-Hm, V_{fb} value moves towards acathodic shift with enhanced of N_d value. Ov-Hm have the highest negative V_{fb} value and the highest N_d value among other catalysts confirming the high electron density and great charge-transfer ability. Thus, high electrocatalytic activity of Ov-Hm is due to the increase of charge-transfer ability and electron density. Thus, higher donor density electrode materials have lower Debye radius. The Debye radius of Ht, Hm and Ov-Hm is 0.76 nm, 0.36 nm, and 0.12 nm, respectively. The smaller Debye radius of Ov-Hm possesses higher charge-transfer ability and higher conductivity.

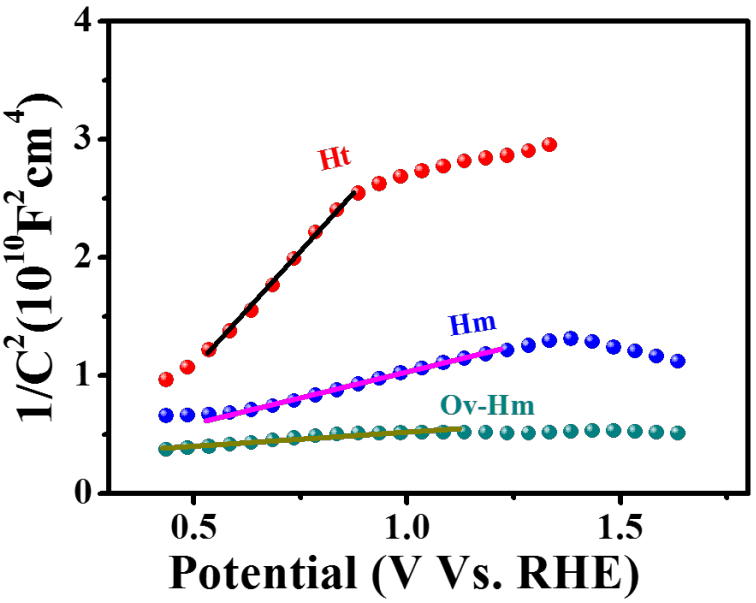

Figure S15. Mott-Schottky plot measured in 10 KHz in 1 M KOH for Ht, Hm and Ov-Hm.

Table S4: Flat Band Potential, Donor Density and Debye radius Values of all the catalysts

Catalysts	**Flat Band Potential (V_{fb}) (V vs. RHE)**	**Donor Density (N_d) (cm^{-3})**	**Debye radius (L_D) (in nm)**
Ht	0.21	9.4×10^{17}	0.76
Hm	-0.20	4.06×10^{18}	0.36
Ov-Hm	-0.82	3.61×10^{19}	0.12

Durability Test of Ov-Hm

In addition to higher activity, operational stability is also an important parameter for promising applications. As Ov-Hm shows excellent activity towards OER, its durability was further accessed (Figure S13). After 5000 cycles of continuous operation, no significant potential degradation (@10 $mAcm^{-2}$) was observed (Figure S13a). During the chronopotentiometric stability test, Ov-Hm exhibited a very steady potentiometric profile with 99 % operational potential retention over 30 h of continuous operation whereas the benchmark catalysts IrO_2/C yields 95 % operational potential retention over only 9 h electrolysis (Figure S13b). This reflects the robustness in the long-term reaction stability of Ov-Hm and will find promising applications in the real field. Since OER is an important application for Fuel cells and metal-air batteries, high efficiency and commercialization of these devices require earth-abundant, low cost and easily available OER catalyst. Therefore, the above observation supports that the Ov-Hm could be the best abundant Fe-based catalyst of choice.

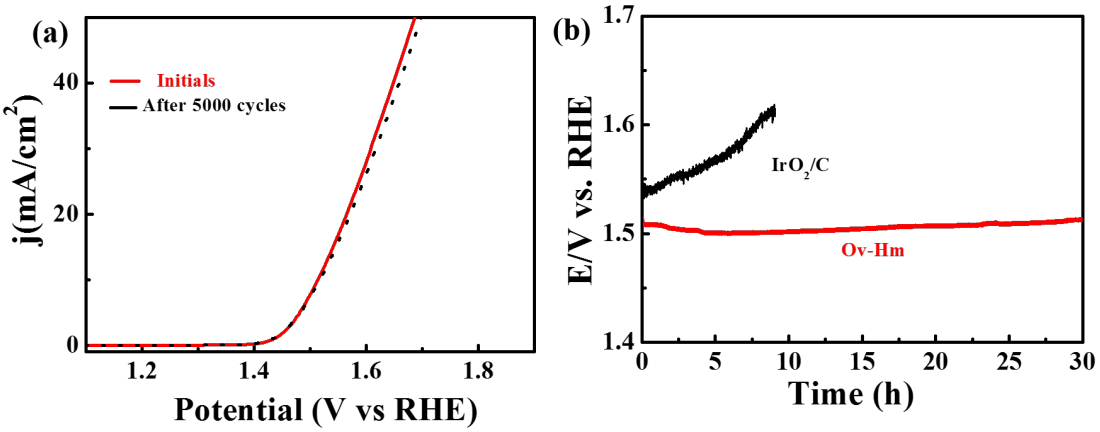

Figure S16: (a) LSV Polarisation plot of Ov-Hm in 1st and 5000th. (b) Durability comparison of Ov-Hm and IrO_2/C at a constant current density of 10 mA/cm^2 for 30 hrs

Characterisation of Ov-Hm before and after stability tests

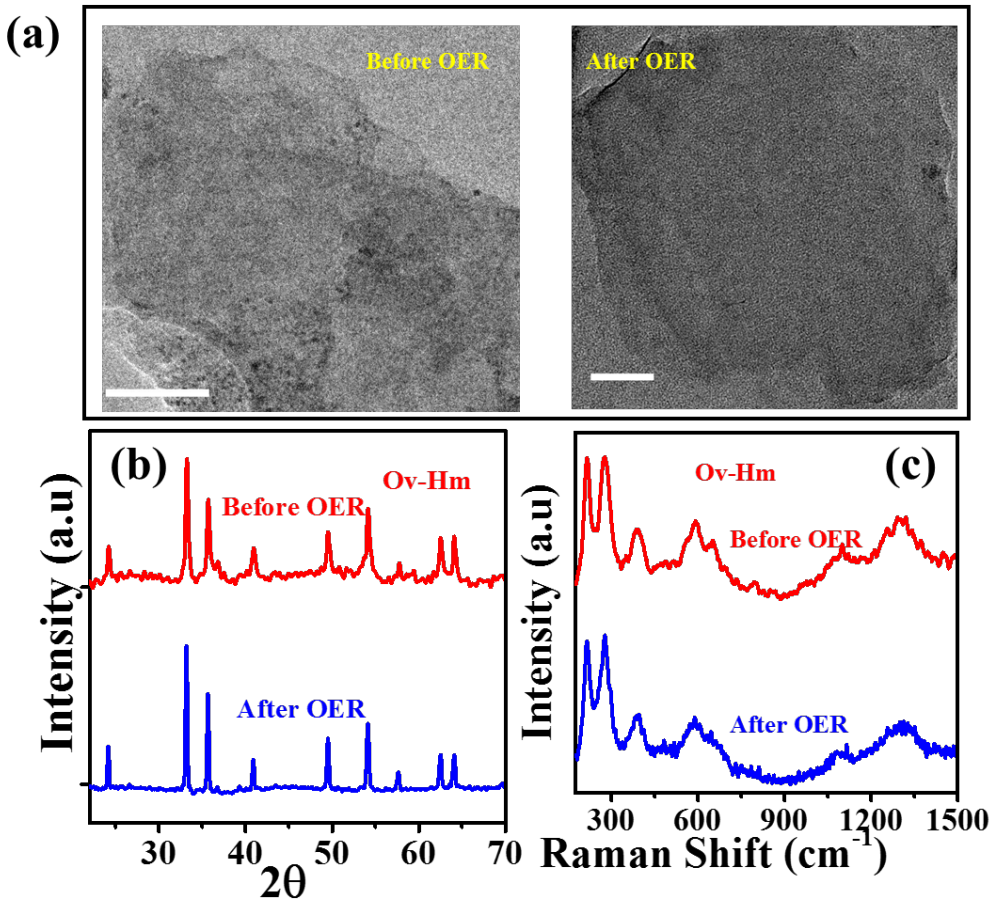

Figure S17: Characterisation of Ov-Hm before and after OER stability measurement; (a) TEM (b) XRD and (c) Raman analysis.

Table S5. The calculated and experimental lattice parameters (in Å) for bulk and monolayer α-Fe_2O_3.

	Present work	Theory [5]	Experiment [12,17]
Ht	a=b=5.07, c=13.88	a=b=5.07, c=13.88	a=b=5.04, c=13.75
Hm	a=b=5.17	-	a=b=5.04

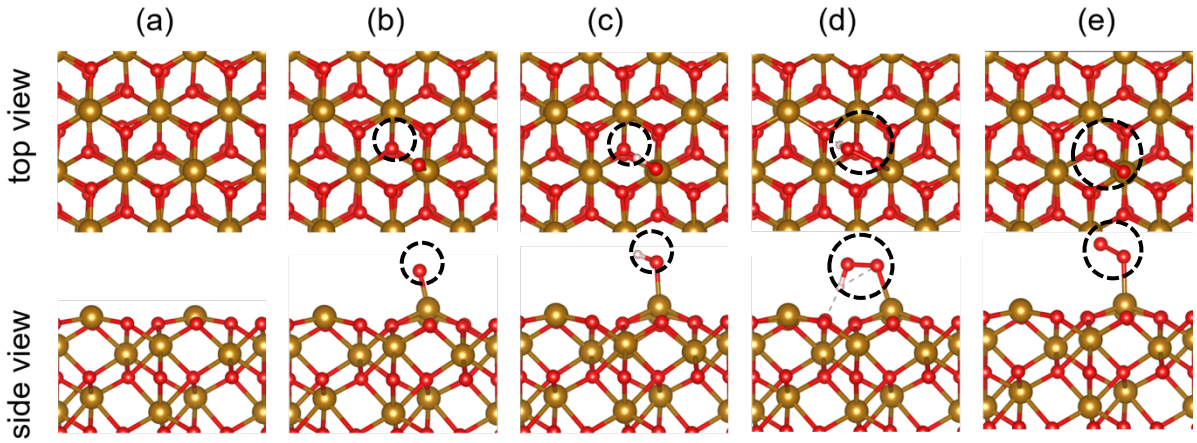

Figure S18. The optimized structures of (001)-Ht for OER. (a) Pristine monolayer and with (b) O* (c) OH* (d) OOH* and (e) OO* adsorption. Brown spheres represent metal ions, red spheres represent oxygen, and white spheres represent hydrogen. Molecules are labeled with black circles.

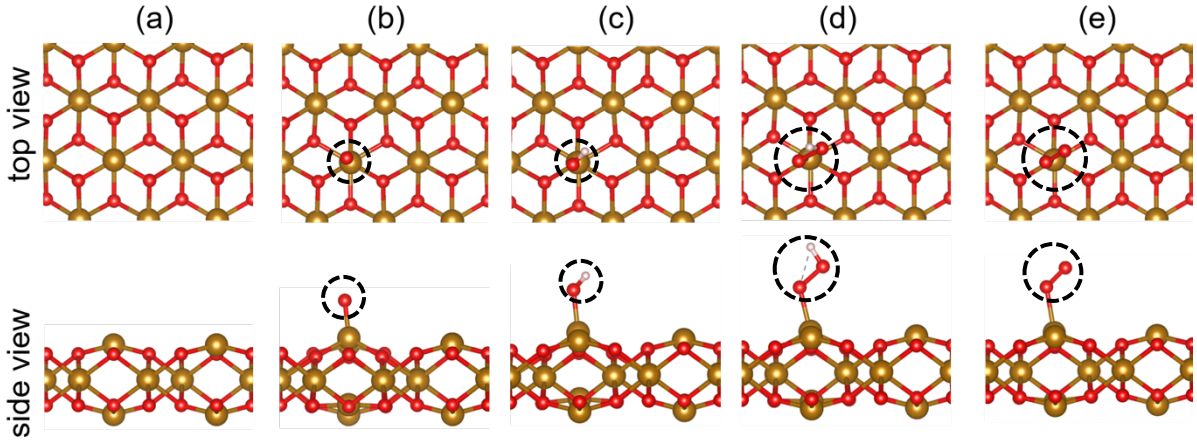

Figure S19. The optimized structures of Hm for OER. (a) Pristine monolayer and with (b) O* (c) OH* (d) OOH* and (e) OO* adsorption. Brown spheres represent metal ions, red spheres represent oxygen, and white spheres represent hydrogen. Molecules are labeled with black circles.

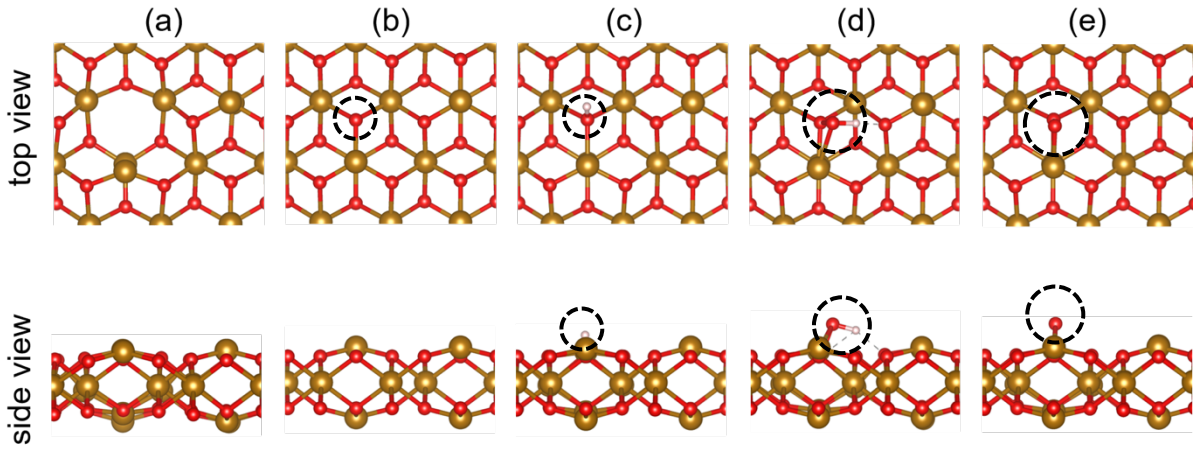

Figure S20. The optimized structures of Ov-Hm for OER. (a) Pristine monolayer and with (b) O*, (c) OH* (d) OOH* and (e) OO* adsorption. Brown spheres represent metal ions, red spheres represent oxygen, and white spheres represent hydrogen. Molecules are labeled with black circles.

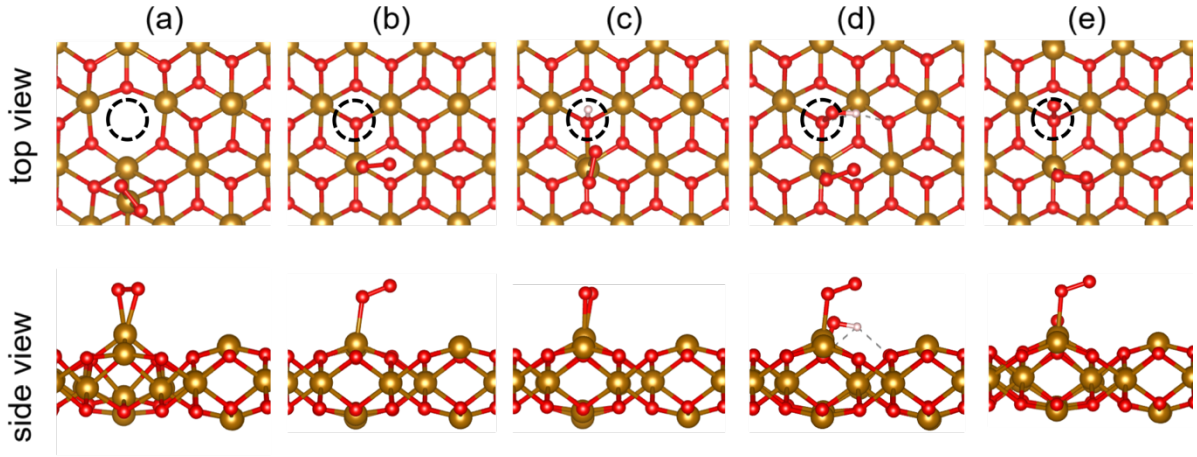

Figure S21. The optimized structures of Ov-Hm with O_2 for OER. (a) Pristine monolayer and with (b) O* (c) OH* (d) OOH* and (e) OO* adsorption. Brown spheres represent metal ions, red spheres represent oxygen, and white spheres represent hydrogen. Molecules are labeled with black circles.

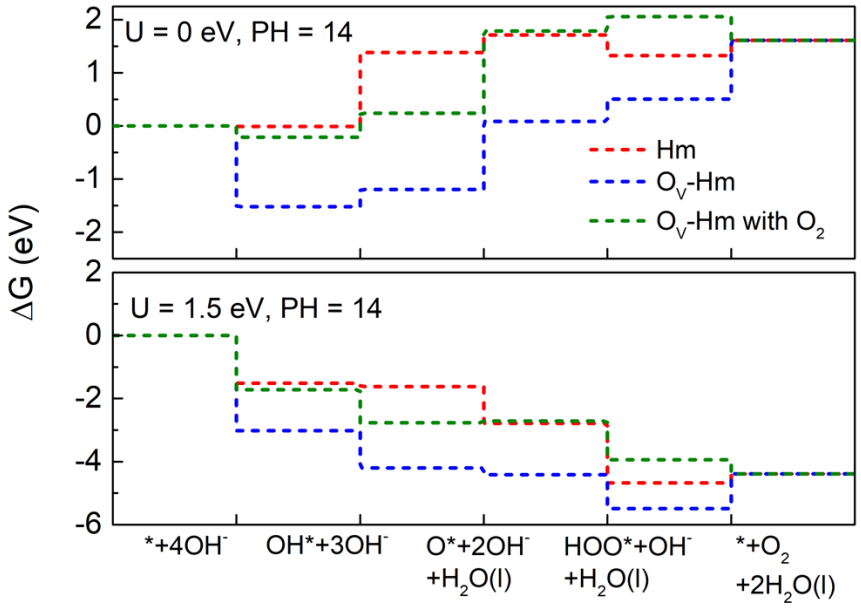

Figure S22. Free energy profiles for OER on Hm, O_v-Hm and O_v-Hm with O_2. The results are obtained at external potential U_{ext} = 0.0, 1.5 V and pH = 14.

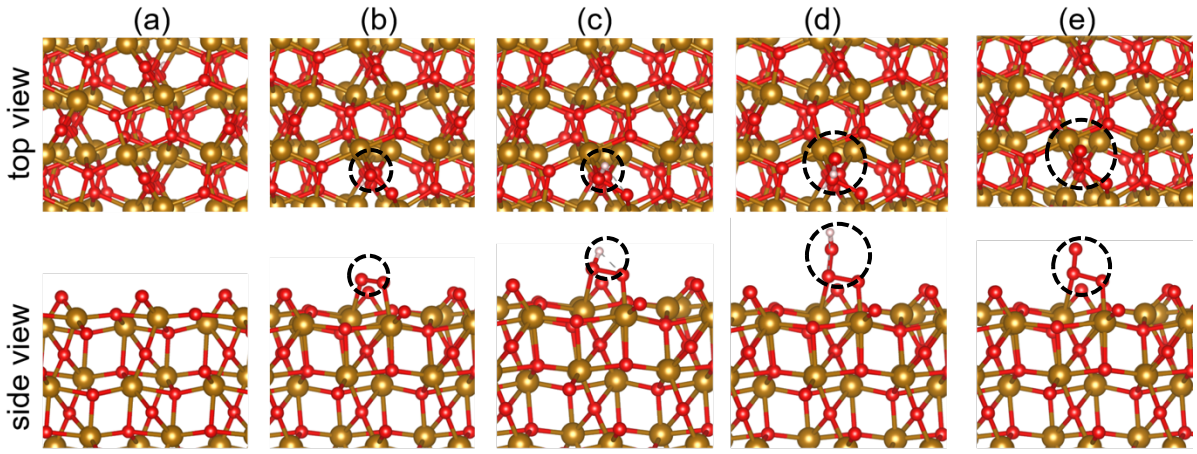

Figure S23. The optimized structures of (104)-Ht for OER. (a) pristine monolayer and with (b) O* (c) OH* (d) OOH* and (e) OO* adsorption. Brown spheres represent metal ions, red spheres represent oxygen, and white spheres represent hydrogen. Molecules are labeled with black circles.

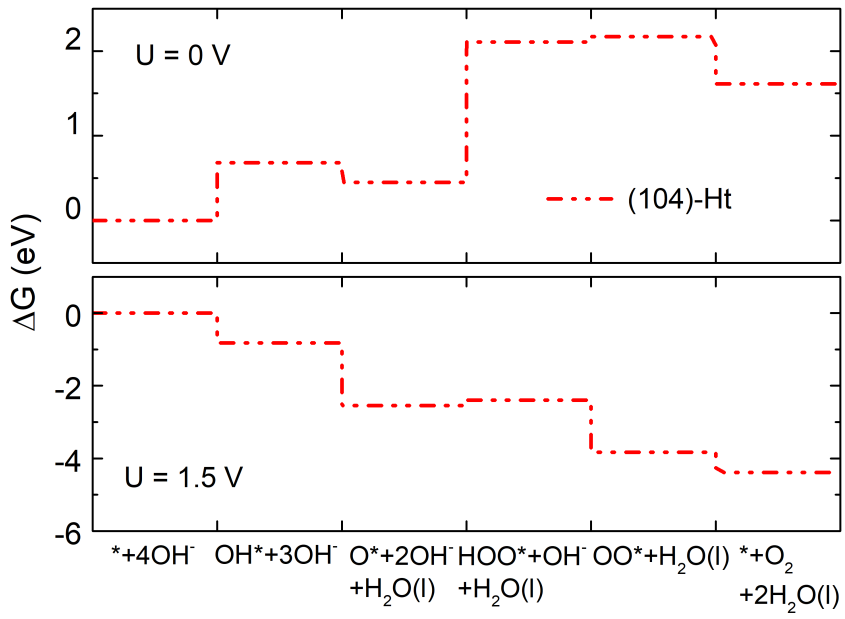

Figure S24. Free energy profiles for OER on (104)-Ht. The results are obtained at external potential U_{ext} = 0.0, 1.5 V and pH = 14.

Table S6. The calculated OER overpotentials on (001), (104)-Ht and Hm and (110)-IrO_2.

Material	η^{OER}
(001)-Ht	1.59
Hm	1.39
O_V-Hm	1.28
(104)-Ht	1.66
(110)-IrO_2[28-30]	1.73-1.98

Table S7. The absolute charge ($|e^-|$) of intermediates on Hm and O_V-Hm.

	Hm	O_V-Hm
O	0.072	0.025
OH	0.166	0.033
OOH	0.162	0.024
OO	1.18	0.541

References

1 H. Wu, T. Yang, Y. Du, L. Shen and G. W. Ho, *Adv. Mater.*, 2018, **30**, 1804341.

2 L. Zhuang, L. Ge, Y. Yang, M. Li, Y. Jia, X. Yao and Z. Zhu, *Adv. Mater.*, 2017, **29**, 1606793--n/a.

3 A. Dutta, A. K. Samantara, S. K. Dutta, B. K. Jena and N. Pradhan, *ACS Energy Lett.*, 2016, **1**, 169–174.

4 B. Zhang, X. Zheng, O. Voznyy, R. Comin, M. Bajdich, M. García-Melchor, L. Han, J. Xu, M. Liu, L. Zheng, F. P. García de Arquer, C. T. Dinh, F. Fan, M. Yuan, E. Yassitepe, N. Chen, T. Regier, P. Liu, Y. Li, P. De Luna, A. Janmohamed, H. L. Xin, H. Yang, A. Vojvodic and E. H. Sargent, *Science*, 2016, **352**, 333 LP – 337.

5 J.-Y. Zhang, L. Lv, Y. Tian, Z. Li, X. Ao, Y. Lan, J. Jiang and C. Wang, *ACS Appl. Mater. Interfaces*, 2017, **9**, 33833–33840.

6 F. Song, W. Li, J. Yang, G. Han, P. Liao and Y. Sun, *Nat. Commun.*, 2018, **9**, 4531.

7 U. Kayal, B. Mohanty, P. Bhanja, S. Chatterjee, D. Chandra, M. Hara, B. Kumar Jena and A. Bhaumik, *Dalton Trans.,* 2019, **48**, 2220–2227.

8 Y. Yao, S. Hu, W. Chen, Z.-Q. Huang, W. Wei, T. Yao, R. Liu, K. Zang, X. Wang, G. Wu, W. Yuan, T. Yuan, B. Zhu, W. Liu, Z. Li, D. He, Z. Xue, Y. Wang, X. Zheng, J. Dong, C.-R. Chang, Y. Chen, X. Hong, J. Luo, S. Wei, W.-X. Li, P. Strasser, Y. Wu and Y. Li, *Nat. Catalysis*, 2019, **2**, 304–313.

9 S. Zhao, Y. Wang, J. Dong, C.-T. He, H. Yin, P. An, K. Zhao, X. Zhang, C. Gao, L. Zhang, J. Lv, J. Wang, J. Zhang, A. M. Khattak, N. A. Khan, Z. Wei, J. Zhang, S. Liu, H. Zhao and Z. Tang, *Nat. Energy*, 2016, **1**, 16184.

10 K. Gelderman, L. Lee and S. W. Donne, *J. Chem. Educ.* , 2007, **84**, 685.

11 S. Bolar, S. Shit, J. S. Kumar, N. C. Murmu, R. S. Ganesh, H. Inokawa and T. Kuila, *Appl. Catal. B: Environ.*, 2019, **254**, 432–442.

12 G. Kresse and J. Hafner, *Phys. Rev. B*, 1993, **47**, 558–561.

13 G. Kresse and J. Hafner, *Phys. Rev. B*, 1993, **48**, 13115–13118.

14 G. Kresse and J. Furthmüller, *Comput. Mater.*, 1996, **6**, 15–50.

15 J. P. Perdew, K. Burke and M. Ernzerhof, *Phys. Rev. Lett.*, 1996, **77**, 3865–3868.

16 H. J. Monkhorst and J. D. Pack, *Phys. Rev. B*, 1976, **13**, 5188–5192.

17 A. Kiejna and T. Pabisiak, *J. Phys. Condens. Matter*., 2012, **24**, 95003.

18 B. Mohanty, M. Ghorbani-Asl, S. Kretschmer, A. Ghosh, P. Guha, S. K. Panda, B. Jena, A. V Krasheninnikov and B. K. Jena, *ACS Catal.*, 2018, **8**, 1683–1689.

19 T. Ungár, *Scripta Materialia*, 2004, **51**, 777–781.

20 A. Banerjee, V. Aravindan, S. Bhatnagar, D. Mhamane, S. Madhavi and S. Ogale, *Nano Energy*, 2013, **2**, 890-896.

21 D. Bersani, P. P. Lottici and A. Montenero, *J. Raman Spectrosc*, 1999, **30**, 355–360.

22 X. Xiang, Z. Wang, X. Shi, M. Fan and X. Sun, *ChemCatChem*, 2018, **10**, 4530–4535.

23 T. Yamashita and P. Hayes, *Appl. Surf. Sci.*, 2008, **254**, 2441–2449.

24 A. Puthirath Balan, S. Radhakrishnan, S. K. Sinha, C. Woellner, L. Deng, C. de los Reyes, M. Banki, M. Paulose, R. Neupane, A. Apte, V. Kochat, R. Vajtai, A. R. Harutyunyan, C.-W. Chu, G. Costin, D. Galvao, A. A. Martí, P. A. van Aken, O. Varghese and P. M Ajayan, *Nat. Nanotechnol.* **13**, 602–609 (2018).

25 C. Dong, T. Kou, H. Gao, Z. Peng and Z. Zhang, *Adv. Energy Mater.*, 2018, **8**, 1701347.

26 X. Lu, Y. Zeng, M. Yu, T. Zhai, C. Liang, S. Xie, M.-S. Balogun and Y. Tong, *Adv. Mater.*, 2014, **26**, 3148–3155.

27 Z. Cai, Y. Bi, E. Hu, W. Liu, N. Dwarica, Y. Tian, X. Li, Y. Kuang, Y. Li, X.-Q. Yang, H. Wang and X. Sun, *Adv. Energy Mater.*, 2018, **8**, 1701694.

28. Gao, J. *et al.* Breaking Long-Range Order in Iridium Oxide by Alkali Ion for Efficient Water Oxidation. J. Am. Chem. Soc. 141, 3014–3023 (2019).

29. Z. Ma *et al.* Reaction mechanism for oxygen evolution on RuO_2, IrO_2, and RuO_2@IrO_2 core-shell nanocatalysts, J. Elect. Chem. 819, 296–305 (2018).

30. Hao, S. *et al.* Tuning Electronic Correlations of Ultra-small IrO_2 Nanoparticles with La and Pt for Enhanced Oxygen Evolution Performance and Long-durable Stability in Acidic Media. *Appl. Catal. B* 266, 118643, (2020).